

Dynamics and Potential Significance of Spontaneous Activity in the Habenula

Suryadi,¹ Ruey-Kuang Cheng,² Elliot Birkett,^{3,4}  Suresh Jesuthasan,^{2,3} and  Lock Yue Chew^{1,5}

<https://doi.org/10.1523/ENEURO.0287-21.2022>

¹School of Physical and Mathematical Sciences, Nanyang Technological University, Singapore 637371, ²Lee Kong Chian School of Medicine, Nanyang Technological University, Singapore 636921, ³Institute of Molecular and Cell Biology, Singapore 138673, ⁴School of Biosciences, University of Sheffield, Sheffield S10 2TN, United Kingdom, and ⁵Complexity Institute, Nanyang Technological University, Singapore 637335

Abstract

The habenula is an evolutionarily conserved structure of the vertebrate brain that is essential for behavioral flexibility and mood control. It is spontaneously active and is able to access diverse states when the animal is exposed to sensory stimuli. Here we investigate the dynamics of habenula spontaneous activity, to gain insight into how sensitivity is optimized. Two-photon calcium imaging was performed in resting zebrafish larvae at single-cell resolution. An analysis of avalanches of inferred spikes suggests that the habenula is subcritical. Activity had low covariance and a small mean, arguing against dynamic criticality. A multiple regression estimator of autocorrelation time suggests that the habenula is neither fully asynchronous nor perfectly critical, but is reverberating. This pattern of dynamics may enable integration of information and high flexibility in the tuning of network properties, thus providing a potential mechanism for the optimal responses to a changing environment.

Key words: avalanche; criticality; dynamics; habenula; reverberation; spontaneous activity

Significance Statement

Spontaneous activity in neurons shapes the response to stimuli. One structure with a high level of spontaneous neuronal activity is the habenula, a regulator of broadly acting neuromodulators involved in mood and learning. How does this activity influence habenula function? We show here that the habenula of a resting animal is near criticality, in a state termed “reverberation”. This pattern of dynamics is consistent with high sensitivity and flexibility, and may enable the habenula to respond optimally to a wide range of stimuli.

Received July 1, 2021; accepted June 27, 2022; First published August 18, 2022.

The authors declare no competing financial interests.

Author contribution: S.J. and L.Y.C. designed research; S., R.-K.C., E.B., and S.J. performed research; S. contributed unpublished reagents/analytic tools; S. and L.Y.C. analyzed data; S., S.J., and L.Y.C. wrote the paper.

This work was funded by the Singapore Ministry of Education through an Academic Research Fund Tier 1 Award (MOE2016-T1-001-152) and a Tier 2 Award (MOE2017-T2-1-058).

Acknowledgments: We thank Dr. Mahathi Ramaswamy, Dr. He Chong, and Dr. Chua Khi Pin for helpful discussions and prior explorations leading to this work.

Correspondence should be addressed to Suresh Jesuthasan at sureshj@ntu.edu.sg or Lock Yue Chew at lockyue@ntu.edu.sg.

<https://doi.org/10.1523/ENEURO.0287-21.2022>

Copyright © 2022 Suryadi et al.

This is an open-access article distributed under the terms of the [Creative Commons Attribution 4.0 International license](https://creativecommons.org/licenses/by/4.0/), which permits unrestricted use, distribution and reproduction in any medium provided that the original work is properly attributed.

Introduction

A defining feature of neural circuits is their flexibility. Although anatomic connectivity does not change rapidly in a mature animal, functional connectivity can change within seconds, enabling animals to quickly alter their behavior to deal with changing circumstances. This is made possible in part by the action of neuromodulators (Getting, 1989; Marder, 2012; Bargmann and Marder, 2013). To ensure that functional connectivity is appropriate for a given condition, the release of neuromodulators is tied to a variety of factors, such as the internal state of the animal, external cues, and perceived reward.

The habenula is an epithalamic structure that receives indirect input from several sensory systems (Stephenson-Jones et al., 2012; Cheng et al., 2017; Zhang et al., 2017),

is stimulated by punishment or absence of an expected reward (Matsumoto and Hikosaka, 2007; Hong and Hikosaka, 2008; Amo et al., 2014), and has activity that is dependent on the circadian clock (Zhao and Rusak, 2005; Baño-Otálora and Piggins, 2017; Basnakova et al., 2021) and stress levels (Authement et al., 2018). It sends output to a number of structures, including the raphe (Wang and Aghajanian, 1977) and the rostromedial tegmental nucleus (Jhou et al., 2009), which regulate the release of serotonin and dopamine, respectively. Thus, the habenula is well positioned to coordinate release of broadly acting neuromodulators based on a variety of factors. The importance of the habenula is illustrated by a range of defects seen in animals with a lesioned habenula, including an inability to cope with changing circumstances (Thornton and Bradbury, 1989) or to learn effectively (Agetsuma et al., 2010; Lee et al., 2010). The habenula is thus required for behavioral flexibility (Palumbo et al., 2020; Hones and Mizumori, 2022).

How does the habenula process information to efficiently influence behavior? Calcium imaging in zebrafish indicates that neural activity in the habenula is sensitive to various features of sensory input. Different concentrations of odors (Krishnan et al., 2014), as well as wavelengths (Lin, 2015) or levels of ambient illumination (Zhang et al., 2017) trigger different patterns of activity. This can be represented as trajectories in state space, with reproducible trajectories for each stimulus, indicating that sensory stimuli are represented by population activity. Additionally, habenula neurons constantly fire action potentials, even in the absence of sensory stimulation. This was demonstrated in rats using electrical recordings of brain slices, and has also been found in the zebrafish, using two-photon calcium imaging of tethered animals (Jetti et al., 2014; Fore et al., 2018), or CaMPARI (Calcium Modulated Photoactivatable Ratiometric Integrator)-based labeling of freely swimming fish (Fosque et al., 2015). This activity is driven by input from the forebrain (Bartoszek et al., 2021).

The dynamics of spontaneous activity can influence how information is processed. For example, it has been suggested that highly decorrelated firing, also termed “asynchronous irregular activity,” allows a network to respond rapidly to new input, as the effects of previous inputs are quickly dissipated (Van Vreeswijk and Sompolinsky, 1996). Alternatively, the network may reside close to a point of phase transition, as proposed by criticality theory (Beggs and Timme, 2012). However, whether such a state exists *in vivo* is controversial (Wilting and Priesemann, 2019b). A third possibility is that the network resides at a near critical yet subcritical point between these two regimes, termed reverberation (Wilting and Priesemann, 2018).

To determine the dynamics of the resting habenula, we assess activity using calcium imaging in the zebrafish. The transparency of this system allows imaging in the intact animal. To mitigate inaccuracies that arise from subsampling (Priesemann et al., 2009; Ribeiro et al., 2014), which can lead to failure to detect criticality, we use the MR estimator that was recently described (Wilting and Priesemann, 2018).

Materials and Methods

Ethical statement

Experiments were conducted using protocols approved by the Institutional Animal Care and Use Committee of Biopolis, Singapore (#171215).

Microscopy and image processing

Calcium imaging was conducted on an upright two-photon microscope system (model A1RMP, Nikon) with a 25× water-immersion objective. Fish expressing nuclear-localized GCaMP6s under the control of the *elav3* promoter [i.e., *Tg(elav3:H2B-GCaMP6s)*; Dunn et al., 2016; age, 7–11 d] were embedded dorsal up in 2% agarose. At this age, sex cannot be determined (Santos et al., 2017). Time-lapse images were collected with no delay between frames, using a resonant scanner. A single plane was recorded at 113 Hz ($n=2$) or ~15 Hz ($n=16$) for 10–15 min. The x - y spatial resolution was 0.50 $\mu\text{m}/\text{pixel}$ for 113 Hz data and 0.33 $\mu\text{m}/\text{pixel}$ for ~15 Hz data.

All processing steps for the recordings, including motion correction and detection of regions of interest (ROIs), were done using suite2p (Pachitariu et al., 2017) with the ROIs subsequently manually curated to exclude neurons outside the region of the habenula. From the fluorescence signals obtained via suite2p, the corresponding $\Delta F/F$ traces were then computed (Jia et al., 2011), following which discrete spikes were inferred using MLspike with gCaMP6s parameters given in the article (Deneux et al., 2016). Over all of the recordings, the number of neurons range from 152 to 252 with a mean value of 205.6.

Avalanche analysis

Neuronal avalanches were computed by summing the neural spike activities across the population, with individual avalanches being separated by periods of silent time bins (i.e., with zero activity). The total number of spikes across one avalanche constitutes the size, while the duration measures the number of time points the avalanche lasts. The power law distribution was fitted and compared against the exponential distribution using the powerlaw package (Alstott et al., 2014). As the mean size given the duration is not a probability distribution, the function was fitted with a simple linear regression in the log scale.

Shape collapse was performed by adapting the procedure described in the study by Marshall et al. (2016) into Python. We began by excluding avalanches whose durations are less than five timesteps, as well as durations whose total number of avalanche samples are less than three. This was followed by computing the average avalanche profile for all durations, after which the durations were rescaled to one. Next, linear interpolation was performed for each avalanche profile at 1000 points across the rescaled duration. This allows the computation of the variance across avalanche profiles through the interpolated points. The shape collapse error could then be computed, defined as the ratio between the mean variance and the squared span of the avalanche profiles. Here the span refers to the difference between the maximum and minimum values over all the avalanche profiles. Using this shape collapse

error, we then searched for the parameter γ that minimizes the shape collapse error in the interval $0 \leq \gamma \leq 5$ in increasing precision: first in steps of 0.1, then 0.01, and last 0.001.

Branching parameter estimation

A branching process is defined as a process where the number of active units in the next timestep A_{t+1} (i.e., descendants) is on average a constant multiple of the active units in the current timestep A_t (i.e., ancestors). We denote this constant m , which is also called the branching parameter. Mathematically we represent it as follows:

$$\langle A_{t+1} | A_t \rangle = mA_t + h, \quad (1)$$

where h represents the mean rate of an external drive coming from outside the branching dynamics, which in the brain may come from stimuli or other brain regions. As the equation suggests, the branching parameter m determines the stability of the dynamics, ranging from one with exponential decay ($m < 1$) to exponential growth ($m > 1$). $m = 1$ then denotes the critical boundary between the two dynamics, which is where critical avalanches in neuronal systems are said to lie in the study by Beggs and Plenz (2003).

Under spatial subsampling, the conventional way of simply regressing the time series at one timestep apart (i.e., A_{t+1} against A_t) fails to accurately determine m . Here we make use of the multistep regression (MR) estimator of m that has been proven to be consistent even under severe binomial subsampling (Wilting and Priesemann, 2018). To do so, linear regressions were performed for all pairs of A_{t+k} against A_t for all $k = 1, \dots, k_{\max}$ to obtain slopes r_k . It has been shown that while under full sampling we have $r_k = m^k$, subsampling leads to a constant bias for the slope r_k at all values of k (Wilting and Priesemann, 2018), as follows:

$$r_k = bm^k. \quad (2)$$

The true m can then be readily estimated by curve fitting r_k against k using this equation. We note that since $0 \leq m \leq 1$, this relation is in general an exponential decay function, except when $m = 0$ or 1 . m^k can also be rewritten as $e^{-k\Delta t / \tau}$ (Wilting and Priesemann, 2018), where $\tau = -\Delta t / \log m$ denotes the autocorrelation time of the process and Δt is the timescale of the data (i.e., the time interval between each measured timestep). τ diverges at criticality (when $m = 1$), and otherwise still yields information about the timescale at which the influence of a perturbation remains in the system.

Tests on nonstationarity and Poisson activity

As with most statistical estimations for time series, this estimator is valid only when the time series is stationary. We applied a series of tests to identify common sources of nonstationarities (tests 1–3) and to check for the possible presence of Poisson activity (test 4; Wilting and Priesemann, 2018). Our aim was to ensure that the branching process is able to describe the dynamics present in the data. The following was done. (1) We tested the original exponential model $r_k = b \cdot m^k$ against the

exponential model $r_k = b_{\text{offset}} \cdot m_{\text{offset}}^k + c_{\text{offset}}$, with offset c_{offset} accounting for a transient increase in the drive. If the residual of the fit with offset R_{offset}^2 was smaller than the residual of the original model R_{exp}^2 by a factor of two, $H_{\text{offset}} = (2 \cdot R_{\text{offset}}^2 < R_{\text{exp}}^2)$, we rejected the dataset. (2) We compared the relative difference between the autocorrelation time τ of the original exponential model and the above exponential model with offset to detect ramping of the drive. If the difference was too large, $H_{\tau} = (|\tau_{\text{exp}} - \tau_{\text{offset}}| / \min\{\tau_{\text{exp}}, \tau_{\text{offset}}\} > 2)$, we again deduced the invalidity of the MR estimation. (3) If the linear regression model $r_k = q_1 k + q_2$ gave a better fit of r_k against k compared with the original exponential model such that the residuals R_{lin}^2 was smaller than R_{exp}^2 : $H_{\text{lin}} = (R_{\text{lin}}^2 < R_{\text{exp}}^2)$, we rejected the data and concluded that the presence of sudden jumps in the drive were due to state changes. (4) We performed a one-sided t test to determine whether the mean of r_k is significantly larger than zero, which is useful when r_k appears as a flat line as it may result from both critical ($m = 1, r_k > 0$) and Poisson ($m = 0, r_k = 0$) cases. The t test returns a p -value $p_{\bar{r} < 0}$, through which we define a test $H_{\text{MR_invalid}} = (p_{\bar{r} < 0} \geq 0.1)$. If $H_{\text{MR_invalid}}$ is positive, Poisson activity is then confirmed by performing an additional test to ensure that no systematic trend exists in r_k . This is done via the above linear regression model by showing that r_k has slope q_1 zero with $H_{\text{poisson}} = (p_{q_1=0} \geq 0.05)$. Datasets that are positive for both $H_{\text{MR_invalid}}$ and H_{poisson} are explained by Poisson activity, while those positive for $H_{\text{MR_invalid}}$ but not H_{poisson} are not Poisson but are nevertheless invalid for MR estimation.

Nonstationarities are uncovered when any of the computed H_{offset} , H_{τ} , or H_{lin} values is positive. MR estimation is considered valid when H_{offset} , H_{τ} , H_{lin} , and $H_{\text{MR_invalid}}$ values are all negative (regardless of H_{poisson}). When both $H_{\text{MR_invalid}}$ and H_{poisson} values are positive, the procedure is valid with the conclusion that the system exhibits Poisson activity (i.e., $m = 0$). On the other hand, if $H_{\text{MR_invalid}}$ is positive but H_{poisson} is negative, then MR estimation is not valid and no further conclusion can be made on the activity.

Spike count covariance

The spike count covariance was computed as described in the study by Dahmen et al. (2019). First, each dataset was divided into N subsets, and the total activity was computed for each neuron in each subset, which we denoted as n_i^p , where i denotes the neuron and $p = 1, \dots, N$ denotes the subset. We then computed for each combination of subsets the unbiased estimator for the covariance between neuron i and neuron j , as follows:

$$\hat{c}_{ij} = \frac{1}{N-1} \sum_{p=1}^N (n_i^p - \bar{n}_i) (n_j^p - \bar{n}_j), \quad (3)$$

where $\bar{n}_i = \frac{1}{N} \sum_{p=1}^N n_i^p$ denotes the average total activity of neuron i over the different subsets. The corresponding

spike count correlation could be computed by dividing each \bar{n}_i by the square root of its variance $\sqrt{\widehat{c}_{ii}}$. The dimensionality N_{eff} of the activity could be measured via the participation ratio (Abbott et al., 2011; Mazzucato et al., 2016). This is determined by performing principal component analysis (PCA) on the spike count matrix, and calculating the following:

$$N_{\text{eff}} = \left(\sum_{k=1}^K \tilde{\lambda}_k^2 \right)^{-1}, \quad (4)$$

with $\tilde{\lambda}_k$ being the explained variance ratio of the k th principal component.

We can probe how far the system is to the dynamically balanced critical state through λ_{max} , which measures the largest (and therefore most unstable) eigenvalue of the underlying connectivity matrix of the network. The critical point occurs at $\lambda_{\text{max}} = 1$. It is given by Dahmen et al. (2019), as follows:

$$\lambda_{\text{max}} = \sqrt{1 - \sqrt{\frac{1}{1 + N\Delta^2}}}, \quad (5)$$

where $\Delta = \delta c_{ij}/c_{ij}$ is the normalized width of the spike count covariance distribution with δc_{ij} being the SD of the covariance distribution, and N is the underlying network size, which we take to be 1500 for the larval zebrafish habenula (Pandey et al., 2018). A limited amount of data incurs bias in the estimation of the width; an extensive discussion on the bias and its correction can be found in the study by Dahmen et al. (2019).

Data availability

Multistep regression was performed using the MR estimator toolbox (Spitzner et al., 2021). The remaining codes used for computation in this study are available at GitHub (https://github.com/suryadi-t/reverberating_habenula). All computations were performed on an HP Z440 Workstation (3.70GHz CPU) with the 64 bit Windows 10 Education OS.

Results

Analysis of avalanches fails to provide evidence of criticality

We first asked whether there is evidence for criticality in the habenula. One signature of criticality is the presence of neuronal avalanches, which is defined as cascades of neuronal activity between periods of silence, with duration and size distributions exhibiting power laws. Two-photon calcium imaging was used to monitor spontaneous activity in the zebrafish habenula (Fig. 1A), as visible light used in confocal microscopy causes an evoked response (Dreosti et al., 2014). Upon recording a single plane of neurons in the habenula (at ~ 15 Hz) and using MLspike to infer spiking activity in the neurons, we found that at least one neuron was active at any given frame for all 16 recordings (Fig.

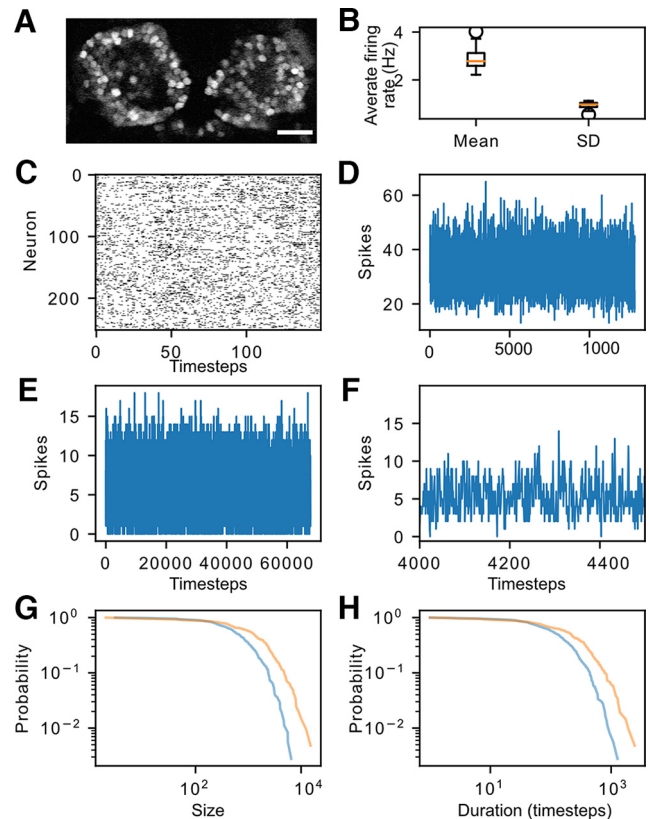


Figure 1. Characterization of neuronal avalanches in the habenula. **A**, The habenula of *Tg(ela13:H2B-GCaMP6s)* fish, imaged at 15 Hz. Scale bar, 25 μm . **B**, Population statistics (mean and standard deviation, SD) of the neuron average firing rate aggregated over all recordings. The individual firing rate distributions for each recording are given in Extended Data Figure 1-1. **C**, Activity in a subset of neurons in the habenula imaged at 15 Hz. The black lines indicate frames where there is at least one spike inferred by MLspike. **D**, Plot showing number of spikes across the population as inferred by MLspike. **E**, **F**, Inferred spikes, obtained from imaging a single plane at 113 Hz. **E** is the entire recording, whereas **F** is a zoomed in version to a portion. **G**, **H**, Distribution of avalanche size (**G**) and duration (**H**) in fish imaged at 113 Hz at a single plane. The blue curve is based on data from one fish, while the orange curve is derived from a second fish. The log-log plots are not linear, indicating the absence of a power law. Further avalanche analyses are given in Extended Data Figure 1-2.

1C,D). This lack of silent time bins, which implies a lack of avalanches, could be because of the slow rate of recording. We thus made additional recordings at 113 Hz. These yielded periods of inactivity (Fig. 1E,F): two 10 min recordings yielded 360 and 207 distinct avalanches. These observations suggest that avalanches exist in the habenula.

It is predicted from scaling theory (and verified experimentally) that critical avalanching systems manifest power law distributions for both the avalanche size (S) and duration (T ; Beggs and Plenz, 2003). In addition, the mean avalanche size given duration $\langle S \rangle(T)$ also follows a power law (Friedman et al., 2012). These are summarized below:

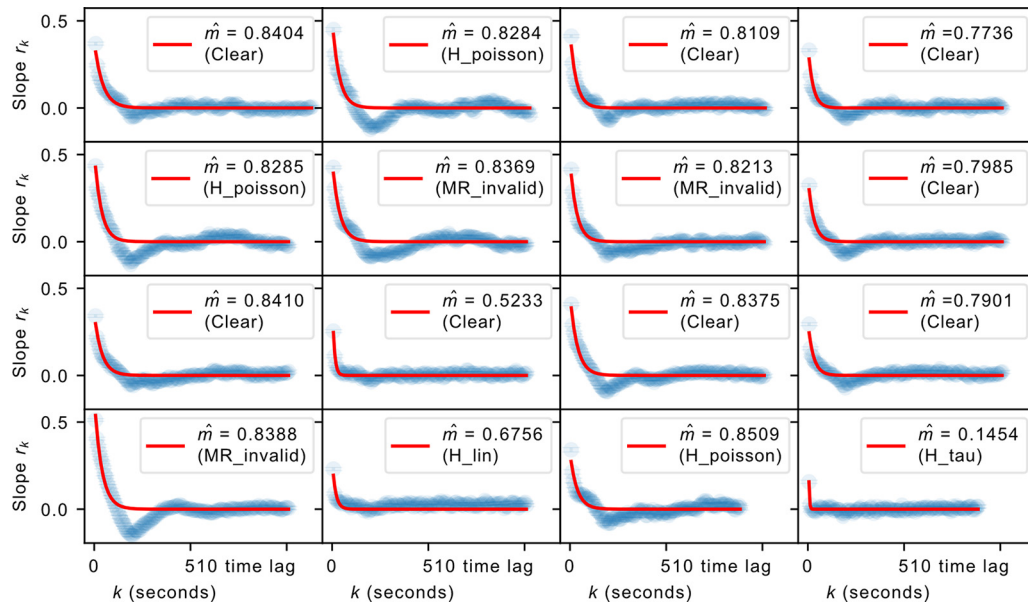


Figure 2. The regression slopes r_k at different time lags k . The blue curve represents actual data, whereas the red curve is the fit using the estimated \hat{m} based on Equation 2. The value of the estimated \hat{m} is shown alongside the results for stationarity tests—datasets that pass all the tests are denoted as Clear while those that fail at least one are indicated by the first test they failed. For relatively short datasets, even a stationary branching process can test positive for H_{poisson} and $H_{\text{MR_invalid}}$, as shown in Extended Data Figure 2-1.

$$f(S) \sim S^{-\tau}, \tag{6}$$

$$f(T) \sim T^{-\alpha}, \tag{7}$$

$$\langle S \rangle(T) \sim T^\beta. \tag{8}$$

When analyzed with the powerlaw package (Alstott et al., 2014), the size and duration of these avalanches did not fit a power law (Fig. 1G,H; likelihood ratio test did not favor power law over exponential distribution for all cases with $p > 0.1$). While we observe that Equation 8 appears to hold in this system (Extended Data Fig. 1-2), this relation is known to be valid quite far from criticality (Friedman et al., 2012), and is therefore insufficient on its own to demonstrate criticality. This can be analyzed further by inspecting the avalanche shape (Extended Data Fig. 1-2). A critical system exhibits self-similarity, which manifests not only power law avalanche distributions, but also avalanche shapes that are, on average, identical across scales. Mathematically, the mean number of spiking neurons $s(t, T)$ at the t th time instant in an avalanche of duration T relates to a universal profile $F(t/T)$ as follows:

$$s(t, T) \propto T^\gamma F(t/T). \tag{9}$$

By rescaling the durations, these avalanches of different durations could then be collapsed into a universal shape by computing $s(t, T)T^{-\gamma}$. In a critical avalanching system, the resulting γ relates to β from Equation 8 in a simple way (Friedman et al., 2012):

$$\gamma = \beta - 1. \tag{10}$$

We observe in our data that while there is an apparent shape collapse, the shape is flat instead of the parabolic

shape predicted by mean field theory, which has also been observed experimentally in neural systems (Friedman et al., 2012; Marshall et al., 2016). In addition, Equation 10 fails to hold here. These observations, particularly the absence of power law distributions in both avalanche size and duration, indicate that the system is not critical.

The MR estimator suggests a subcritical, reverberating state

This lack of evidence for a critical state may be because of subsampling, which was imposed by technical limitations. Specifically, volumetric imaging could not be conducted at a high enough rate, because of delays in focusing across the entire depth of the habenula. We thus used the MR estimator to provide a measure of where the dynamics of the habenula resides in the asynchronous versus critical spectrum. Given that nonstationarities in the data may lead to inaccuracies in the estimation process (Wilting and Priesemann, 2018), we first performed several tests to identify common nonstationarities. These results are indicated in Figure 2, where datasets that passed all stationarity tests are indicated as “Clear” while datasets that did not pass are indicated by the first test they failed. Here the points are expected to follow an exponential decay as given in Equation 2 in the Materials and Methods section, which we observe to be the case, with the red curve in each subplot representing the fit by the exponential decay function. We later show in Extended Data Figure 3-1 that this shape is abolished on temporally shuffling the data.

We found a number of datasets that were positive for H_{poisson} or $H_{\text{MR_invalid}}$. These tests were conducted to identify regimes of Poisson activity for which r_k is expected to be a noisy fluctuation of ~ 0 , in which case the mean of r_k would

naturally not be significantly larger than zero, thereby being positive for the tests. In the datasets that tested positive for $H_{MR_invalid}$ and $H_{poisson}$; however, we observe the characteristic exponential decay in line with the prediction for a non-Poisson and noncritical branching process ($0 < m < 1$), which effectively places these datasets outside of what the two tests are addressing. We therefore hypothesized that these datasets result from stationary branching processes, which are positive for either of the two tests because of fluctuations due to small sample size. This is supported by the observation that the estimated \hat{m} for these datasets are consistent with the other accepted recordings. We then verified this by simulating subsampled stationary branching processes to the same time series length as our data and show that we could indeed observe these cases testing positive for either of the two tests (Extended Data Fig. 2-1). Hence, we chose to proceed with the datasets that either cleared all the stationarity tests or were positive for only $H_{MR_invalid}$ or $H_{poisson}$. We subsequently refer to these datasets as accepted datasets.

The accepted datasets were analyzed with the MR estimator, with the results also indicated in Figure 2. The dynamics of the habenula was treated as a branching process, such that the activity in the next timestep A_{t+1} is on average a linear function of that in the current timestep with the addition of some external drive with a mean rate h , as given in Equation 1. As the equation indicates, m encodes the amount of temporal correlation present in the system; the spatial correlation is implicit as this framework considers not individual units, but the total activity over the entire system. When measured in the timescale of neuron activity, $m = 0$ denotes a state with no temporal correlation (i.e., asynchronous-irregular), while $m = 1$ denotes a critical state where long-term temporal correlation is observed. When m is close to but not exactly 1 in the neuron activity timescale, the system is situated in a reverberating state that shares some of the benefits of the critical state without its drawbacks (Wilting and Priesemann, 2019b). As m is close to 1 in this regime, it is also characterized by long autocorrelation time.

We emphasize that this reverberating state is assessed from m being close to 1 only when measured at the timescale of neural activity. When measured at slower timescales, the inferred value of m changes as it depends on the sampling rate. Specifically, data arising from stationary branching processes should display the branching activity in a systematic way across different timescales within the limits of its autocorrelation time. At different measurement time bins Δt , the inferred branching parameter \hat{m} at the time scale of Δt should relate to the true branching parameter m_{true} at the actual timescale of the underlying process ΔT as follows:

$$\hat{m} = m_{true}^{\Delta t / \Delta T} = \phi^{\Delta t}, \quad (11)$$

where we have $\phi = m_{true}^{1/\Delta T}$ grouping the two unknown constants together as they cannot be estimated separately from data. We studied whether this relation holds for our datasets by temporally subsampling our recordings and rerunning the pipeline in each iteration (i.e., $\Delta F/F$ computation, MLspike inference, stationarity tests, and

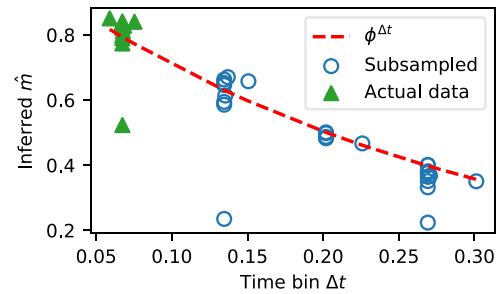


Figure 3. Inferred \hat{m} values of the accepted datasets as well as temporally subsampled data. There is a systematic downward trend with increasing time bin Δt size consistent with theoretical expectations. The theoretical fit (without the three outliers) is shown as a red dashed line. This trend is not by chance, as time-shuffled data indicate Poisson activity regardless of Δt (Extended Data Fig. 3-1).

computation of \hat{m}). The results are given in Figure 3, where we show the inferred \hat{m} values obtained from the accepted datasets alongside temporally subsampled data that pass the stationarity tests. Here we see a downward trend relative to increasing time bins that is generally consistent with Equation 11. This consistency supports the validity of the branching process and MR estimator in describing the dynamics in the habenula, as the change in \hat{m} across different time bins is consistent with theoretical expectation. Excluding the three outliers, fitting Equation 11 to Figure 3 yields $\phi = 0.0326$, which when converted to the timescale of $\Delta T = 4$ ms to reflect the true neural activity timescale (Wilting and Priesemann, 2019a) gives us $\hat{m} = 0.986$, which is indeed in the reverberating regime. This is consistent with studies on mammalian cortex in the reverberating regime, which when measured at $\Delta t = 4$ ms yielded \hat{m} in the range of 0.963–0.998 with a median of 0.980 (Wilting and Priesemann, 2019a). On the other hand, Equation 11 also indicates what happens when the system is critical. As is to be expected, a critical system exhibits self-similarity across scales, and Equation 11 shows that when $m_{true} = 1$, $\hat{m} = 1$ across different Δt , which is not the case in the habenula. Lastly, we note that the systematic relationship shown in Figure 3 is not simply a product of chance, as the majority of the time-shuffled counterparts identically display Poisson activity with $\hat{m} = 0$ (Extended Data Fig. 3-1), with the remaining few being positive for other nonstationarities.

Since the estimator has been shown to be generally consistent over spatial subsampling in the cortex of mammals using electrical recordings (Wilting and Priesemann, 2018, 2019a), we tested whether this also holds here with calcium imaging data. Interestingly, we observe that to be not the case, as seen in Figure 4. To understand why, we simulated stationary branching processes at $m_{true} = 0.985$ and 0.9999 , where the two cases reflect reverberating and critical dynamics, respectively. This is followed by temporal subsampling by a factor of 15, as neural activity timescale is approximately $\Delta T = 4$ ms (Wilting and Priesemann, 2019a); this temporal subsampling then brings the measurement timescale to be at $\Delta t = 60$ ms, which is close to that of our recordings (approximately $\Delta t = 66$ – 76 ms). In this coarser

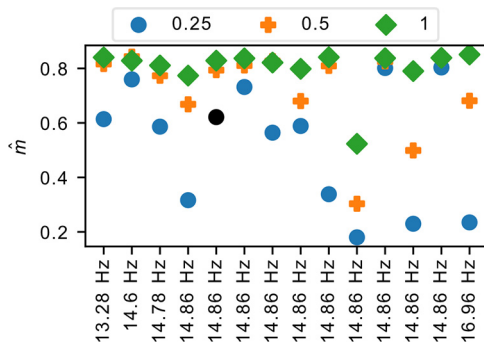


Figure 4. Effect of spatial subsampling on \hat{m} . The estimated branching parameter \hat{m} for each dataset is labeled and ordered by its sampling rate at different subsample ratios. The one point in black failed a stationarity test. We see that, contrary to expectation, there appears to be systematic underestimation of \hat{m} with spatial subsampling. We further investigate this in Extended Data Figure 4-1.

timescale, the effective values of m become $m = 0.7972$ and 0.9985 , respectively, as per Equation 11. We then performed spatial subsampling in two different ways. In the first case, we spatially subsample by binomial subsampling, where each spike has an equal probability of being “skipped” because of subsampling. We used this as a basis since MR estimator was proven to be consistent under this type of subsampling. In the second case, we follow actual experimental conditions where there is systematic subsampling of specific neurons. We do so by simulating a simple lattice network of neurons, each connected to four other neurons, and subsample by measuring only a random subset of the neurons. To mimic our experimental conditions, we first subsample the network to 250 neurons (approximately the number measured by our recordings) before investigating how further spatial subsampling affects the inferred \hat{m} (similar to Fig. 4). We see in Extended Data Figure 4-1 that the MR estimator is consistent in all these cases, as expected.

After verifying this, we reconsidered the process of temporal subsampling compared with our experimental conditions. Temporal subsampling is typically achieved by measuring a subset of the original data. When subsampling by a factor of n , for every n consecutive data points, we measure the n th element and discard the rest. The situation here, however, differs. Because of the slow decay time of gCaMP6s, MLspike would in principle be able to capture the spikes that occur in between time bins. In this case, then, for every n consecutive data points, we measure the sum over all n elements instead, resulting in a form of temporal summation. The right column of Extended Data Figure 4-1 shows the impact of this temporal summation. In most cases, we see that the MR estimator retains its consistency; however, we see in one case that it begins to systematically underestimate m with severe spatial subsampling. This is in fact the case that corresponds most with our setting: $m = 0.7972$ ($m_{\text{true}} = 0.985$) with both temporal summation and systematic subsampling of neurons. The measured \hat{m} , therefore, serves as a lower bound to the

true value, though we also note that between the subsampling factor of 0.5–1 (i.e., 125–250 neurons, which is approximately the range of neurons measured in our recordings), the measured \hat{m} is still very close to the true value; severe underestimation only occurs when <100 neurons were measured. On the other hand, this underestimation also depends on the value of m in the measured timescale. In the case of $m = 0.9985$ ($m_{\text{true}} = 0.9999$), m is close to 1, and we observe that the average effect of spatial subsampling is almost negligible, while the $m = 0.7972$ ($m_{\text{true}} = 0.985$) case leads to a much more pronounced effect. This could be why this effect of spatial subsampling was not significantly observed in other studies where temporal summation may have been used, because in those cases data were collected using electrical recordings measured at a timescale of $\Delta t = 4$ ms, in which case the effective m is close enough to 1 that the effect of spatial subsampling remains small.

On the other hand, it was also noted that when very few neurons were measured, deviations could also come from heterogeneity within the network (Wilting and Priesemann, 2019a). Our simulations here consist of homogeneous neurons (since we used a lattice topology where every neuron is equivalent), indicating that systematic spatial subsampling can also have an effect on \hat{m} estimation in homogeneous networks, provided temporal summation also occurred (which is quite commonly the case in neural data), although heterogeneity would naturally exacerbate the effect. Given the diversity of cell types in the habenula (Pandey et al., 2018), it is also likely that heterogeneity in the neuronal activity also contributed to the observed deviations on significant spatial subsampling.

These findings imply two things. First, our measured \hat{m} is possibly a lower bound to the true value, although our simulations also indicated that at our measured population size, they should nevertheless remain close to the true value. Second, the true value is not at the critical point, as our simulations have shown that significant spatial subsampling should have only a negligible effect when m is critical, which is not observed in our data.

Activity in the habenula has a high autocorrelation time

In the preceding section, we looked at how \hat{m} changes with sampling rate and inferred that the system lies in a reverberating state by computing \hat{m} in the neural activity timescale. Another way to assess the state of the system is to convert \hat{m} into the autocorrelation time, which removes the dependence on sampling rate, thereby allowing a fair comparison between different measurement timescales while also providing a measure of persistence of information in the system. As the name suggests, the reverberating state displays long autocorrelation time where incoming information reverberates in the system before dissipating. This autocorrelation time τ is computed as $\tau = -\Delta t / \log m$ where Δt is the measurement timescale (i.e., time bin; Wilting and Priesemann, 2018). Figure 5 shows the values of τ computed from the

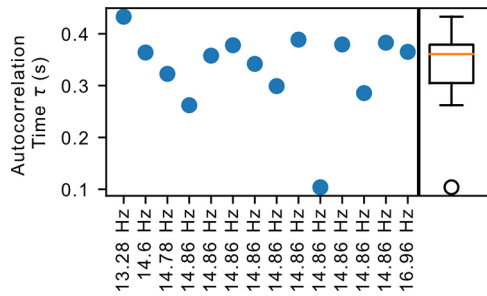


Figure 5. Autocorrelation time in the habenula. The autocorrelation time τ (in seconds) for each of the accepted datasets, labeled and sorted by the recording sampling rate. The box plot on the right shows the aggregated statistics of these values.

accepted datasets, which yielded consistent values ranging from 104 to 433 ms with a mean value of 333 ms (95% CI, 293, 374). The order of magnitude is consistent with τ measured from monkey prefrontal cortex and cat visual cortex, and is an order of magnitude smaller than the τ measured in rat hippocampus; the numerical results across these different systems were jointly reported to cover a range between 100 ms and 2 s with a median value at 247 ms (Wilting and Priesemann, 2019a).

The habenula is reverberating and not critical

We have so far studied the system through the perspective of avalanche distributions and autocorrelation time in branching processes. We asked whether there is additional evidence for the habenula being in a reverberating rather than a critical state. It has been shown that for a state with critical avalanches (i.e., with branching

parameter $m = 1$), the spike count covariance between neurons in the system should be distributed with a mean value far from zero with a relatively small width (Dahmen et al., 2019). What we observe consistently in our system, however, are distributions that are largely symmetrical, ~ 0 (Fig. 6, spike count correlation distribution, which normalized the support of the distribution to $[-1, 1]$). In our datasets, we found that the width is considerably larger than the mean. This finding remains consistent even with further spatial subsampling of the data (Extended Data Fig. 6-1). This is in fact more consistent with another dynamic regime known as the balanced state (Dahmen et al., 2019), which is characterized by an excess of inhibition.

We next looked into the dimensionality of the underlying dynamics. The dynamics of a critical avalanching system is characterized by a single dominant eigenvalue, leading to an effective dimensionality of ~ 1 , which can be probed by performing PCA on the spike count matrix of the system (Dahmen et al., 2019) with the effective dimension computed using the participation ratio (Abbott et al., 2011; Mazzucato et al., 2016). We observed that the habenula datasets display a more gradual decay in the explained variance ratio, which yields a larger effective dimension of $\sim 19.9\text{--}26.9$ (Fig. 7). In addition, the activity along the different principal components are observed to have heterogeneous loadings (Extended Data Fig. 7-1), which contrasts the expected homogeneous loadings for a critical avalanching system (Dahmen et al., 2019). These observations, together with the preceding sections, strongly indicate that the habenula is not in a critical avalanching state. On the other hand, while the findings here may suggest that the habenula could reside in the dynamically balanced critical regime

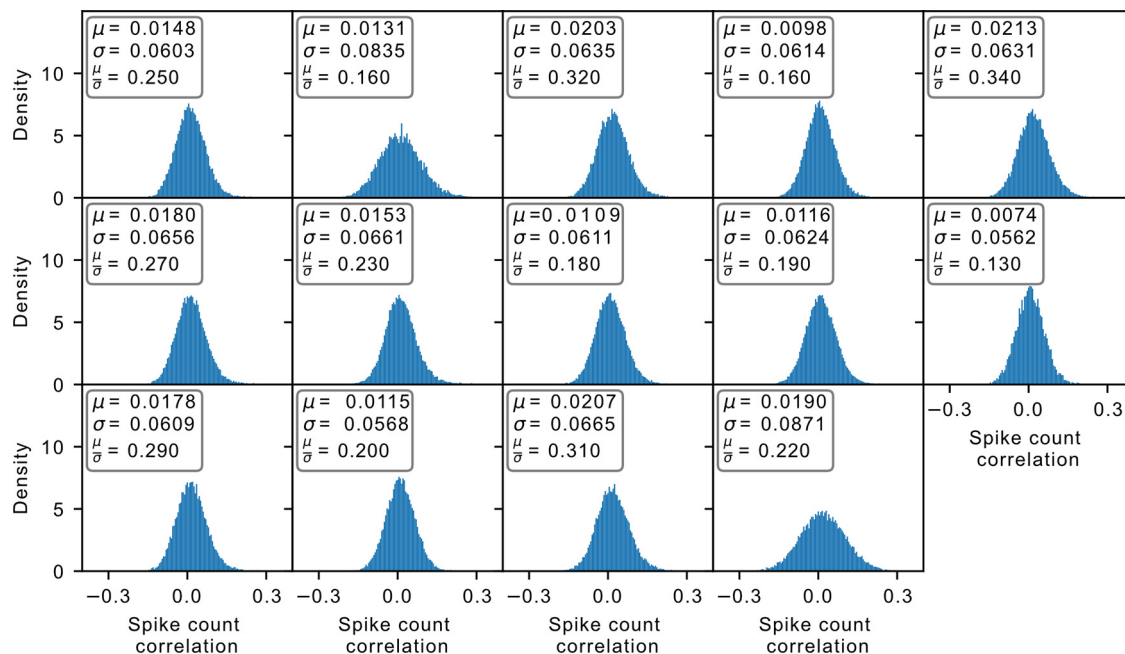


Figure 6. Spike count correlation distribution. Each panel indicates the distribution of a different dataset. For all the accepted datasets, the mean μ is significantly smaller than the width σ of the distribution. This finding is also consistent with further spatial subsampling of the system (Extended Data Fig. 6-1).

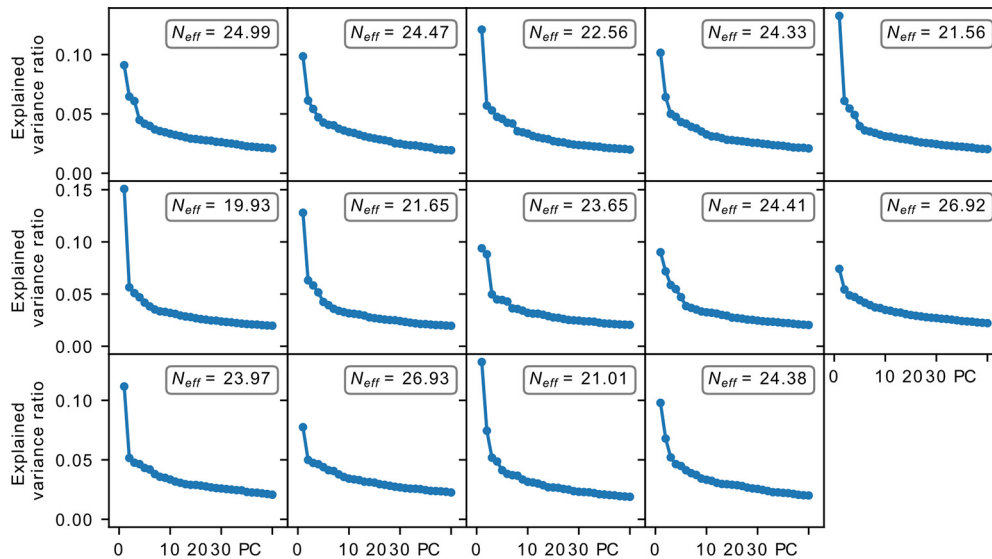


Figure 7. PCA explained variance ratio for the accepted datasets. All cases display a gradual decline instead of just a single dominant contribution, with the effective dimensions being significantly >1 . In addition, activity along the different principal components have heterogeneous loadings (Extended Data Fig. 7-1). These deviate from what is expected from a neural system with critical avalanches.

(the second type of criticality discussed in the study by Dahmen et al., 2019), our analysis revealed that the relevant measure λ_{max} lies significantly below the value that would be expected of such a regime (Fig. 8), indicating that the habenula is also not in the dynamically balanced critical state.

Discussion

The dynamics of a system influences how information is processed. Neural networks have in many instances been described as being either critical (Burns and Webb, 1976; Softky and Koch, 1993) or asynchronous (Van Vreeswijk and Sompolinsky, 1996; Brunel, 2000). The whole zebrafish brain has been suggested to operate at criticality, although regional differences were noted (Ponce-Alvarez et al., 2018). Here, we examined dynamics of the habenula *in vivo*, using calcium imaging at cellular resolution as a

proxy for electrical activity. Through the analysis of avalanches, the autocorrelation time, and population statistics, we found no evidence of criticality, although the system is situated near criticality. And although it does display large fluctuation in population activity and long autocorrelation time, which are signatures of being near avalanche criticality, the habenula also bears features of asynchronous activity in the dynamically balanced state. On the one hand, the spike count covariance distribution of the asynchronous state has a small mean and a large width, in contrast to the large mean and small width of the avalanche critical state (Dahmen et al., 2019). Our analysis indicates that the habenula follows the former statistical behavior of asynchronous state. On the other hand, the asynchronous state is also characterized by weak fluctuations and short autocorrelation time on the population level, and this is where the habenula differs. Thus, our results suggest that the habenula is not exclusively critical or asynchronous.

Existing work on the asynchronous state revealed the existence of a second type of criticality representing the edge of chaos (Dahmen et al., 2019). Such a state is characterized, among others, by multidimensional activity that can be probed using PCA. Each mode of activity (projected to a particular principal component) is realized by a mixture of positive and negative neuron contributions of various magnitudes, which observe long autocorrelation times. In contrast, avalanche criticality has dimension typically ~ 1 , with a single dominant mode given by uniform contribution from all neurons. We observe signs of multidimensional dynamics in the habenula, although we have also shown that the habenula is not situated in this critical point of the second type. Together, our observations indicate that the habenula contains a mixture of characteristics from asynchronous and avalanche dynamics near their respective critical states.

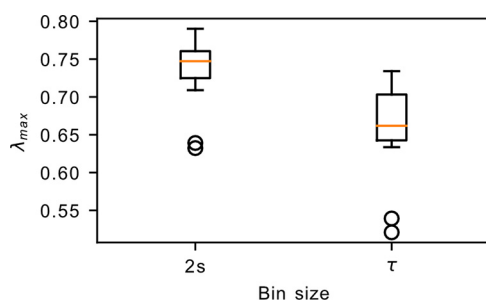


Figure 8. The largest eigenvalue λ_{max} of the connectivity matrix. The computation of λ_{max} requires the binning of the spikes into time bins. This plot shows the results obtained after binning the spikes into 2 s bins, as well as binning into different sizes for each dataset according to its own autocorrelation time τ . In both cases, the λ_{max} values lie well below the critical point at $\lambda_{max} = 1$.

There have been a number of attempts to reconcile the presence of both avalanche and asynchronous dynamics in a network. Simulations show that the incompatible asynchronous and avalanche dynamics can be maintained in the same neuronal network through a balance between excitatory (E) and inhibitory (I) signals at a specified average synaptic strength (Li and Shew, 2020). In other words, a mixture of avalanche and asynchronous neuronal dynamics can result depending on the relative strength of the excitatory and inhibitory synapses (i.e., the I/E weight ratio) and the average synaptic weight. At low I/E weight ratio and weak synaptic strength, the network is near the state of avalanche criticality; while at high I/E weight ratio and strong synaptic strength, it is at the heterogeneous asynchronous state (Ostojic, 2014) near the dynamically balanced critical regime (Dahmen et al., 2019). A system can exhibit characteristics of both avalanching and asynchronous dynamics at a crossover point with a proper balance of E and I (Li and Shew, 2020). This crossover point is not a critical point, which is consistent with what we observe in the habenula.

One interpretation of the dynamics observed is that the habenula is reverberating (Wilting and Priesemann, 2018), as indicated by the inferred m and autocorrelation time. This state is known to combine features from asynchronous and avalanche dynamics (Wilting and Priesemann, 2019a), which has also been observed here in the habenula. The reverberating state, which has been reported previously in mammalian cortical regions, balances the information processing benefits afforded by the critical state, such as sensitivity, but also reduces the drawbacks, such as lower specificity (Wilting and Priesemann, 2019b). A balance of the two may be more optimal for information processing (Wilting et al., 2018). In the reverberating state, small changes in parameter can lead to large changes in the computational properties of the network (Wilting et al., 2018), while the long autocorrelation time may serve as a form of working memory. This is important for adaptation; should there be a sudden change in the environment, the flexibility conferred by the reverberating state will enable optimal change in internal state and thus ensure survival.

References

- Abbott LF, Rajan K, Sompolinsky H (2011) Interactions between intrinsic and stimulus-evoked activity in recurrent neural networks. In: *The dynamic brain: an exploration of neuronal variability and its functional significance* (Ding M, Glanzman DL, eds), pp 1–16. New York: Oxford UP.
- Agetsuma M, Aizawa H, Aoki T, Nakayama R, Takahoko M, Goto M, Sassa T, Amo R, Shiraki T, Kawakami K, Hosoya T, Higashijima S-C, Okamoto H. (2010) The habenula is crucial for experience-dependent modification of fear responses in zebrafish. *Nat Neurosci* 13:1354–1356.
- Alstott J, Bullmore E, Plenz D (2014) powerlaw: a Python package for analysis of heavy-tailed distributions. *PLoS One* 9:e85777.
- Amo R, Fredes F, Kinoshita M, Aoki R, Aizawa H, Agetsuma M, Aoki T, Shiraki T, Kakinuma H, Matsuda M, Yamazaki M, Takahoko M, Tsuboi T, Higashijima S-i, Miyasaka N, Koide T, Yabuki Y, Yoshihara Y, Fukai T, Okamoto H (2014) The habenulo-raphé serotonergic circuit encodes an aversive expectation value essential for adaptive active avoidance of danger. *Neuron* 84:1034–1048.
- Authement ME, Langlois LD, Shepard RD, Browne CA, Lucki I, Kassis H, Nugent FS (2018) A role for corticotropin-releasing factor signaling in the lateral habenula and its modulation by early-life stress. *Sci Signal* 11:aan6480.
- Baño-Otálora B, Piggins HD (2017) Contributions of the lateral habenula to circadian timekeeping. *Pharmacol Biochem Behav* 162:46–54.
- Bargmann CI, Marder E (2013) From the connectome to brain function. *Nat Methods* 10:483–490.
- Bartoszek EM, Ostenrath AM, Jeti SK, Serneels B, Mutlu AK, Chau KTP, Yaksi E (2021) Ongoing habenular activity is driven by fore-brain networks and modulated by olfactory stimuli. *Curr Biol* 31:3861–3874.
- Basnakova A, Cheng RK, Chia JSM, D’Agostino G, Tan GJH, Langley SR, Jesuthasan S (2021) The habenula clock influences response to a stressor. *Neurobiol Stress* 15:100403.
- Beggs JM, Plenz D (2003) Neuronal avalanches in neocortical circuits. *J Neurosci* 23:11167–11177.
- Beggs JM, Timme N (2012) Being critical of criticality in the brain. *Front Physiol* 3:163.
- Brunel N (2000) Dynamics of networks of randomly connected excitatory and inhibitory spiking neurons. *J Physiol Paris* 94:445–463.
- Burns BD, Webb A (1976) The spontaneous activity of neurones in the cat’s cerebral cortex. *Proc R Soc Lond B Biol Sci* 194:211–223.
- Cheng RK, Krishnan S, Lin Q, Kibat C, Jesuthasan S (2017) Characterization of a thalamic nucleus mediating habenula responses to changes in ambient illumination. *BMC Biol* 15:104.
- Dahmen D, Grün S, Diesmann M, Helias M (2019) Second type of criticality in the brain uncovers rich multiple-neuron dynamics. *Proc Natl Acad Sci U|S|A* 116:13051–13060.
- Deneux T, Kaszas A, Szalay G, Katona G, Lakner T, Grinvald A, Rózsa B, Vanzetta I (2016) Accurate spike estimation from noisy calcium signals for ultrafast three-dimensional imaging of large neuronal populations in vivo. *Nat Commun* 7:12190.
- Dreosti E, Llopi N, Carl M, Yaksi E, Wilson SW (2014) Left-right asymmetry is required for the habenulae to respond to both visual and olfactory stimuli. *Curr Biol* 24:440–445.
- Dunn TW, Mu Y, Narayan S, Randlett O, Naumann EA, Yang CT, Schier AF, Freeman J, Engert F, Ahrens MB (2016) Brain-wide mapping of neural activity controlling zebrafish exploratory locomotion. *Elife* 5:e12741.
- Fore S, Palumbo F, Pelgrims R, Yaksi E (2018) Information processing in the vertebrate habenula. *Semin Cell Dev Biol* 78:130–139.
- Fosque BF, Sun Y, Dana H, Yang CT, Ohyama T, Tadross MR, Patel R, Zlatic M, Kim DS, Ahrens MB, Jayaraman V, Looger LL, Schreier ER (2015) Labeling of active neural circuits in vivo with designed calcium integrators. *Science* 347:755–760.
- Friedman N, Ito S, Brinkman BA, Shimono M, DeVille RL, Dahmen KA, Beggs JM, Butler TC (2012) Universal critical dynamics in high resolution neuronal avalanche data. *Phys Rev Lett* 108:208102.
- Getting PA (1989) Emerging principles governing the operation of neural networks. *Annu Rev Neurosci* 12:185–204.
- Hones VI, Mizumori SJ (2022) Response flexibility: the role of the lateral habenula. *Front Behav Neurosci* 16:852235.
- Hong S, Hikosaka O (2008) The globus pallidus sends reward-related signals to the lateral habenula. *Neuron* 60:720–729.
- Jeti SK, Vendrell-Llopi N, Yaksi E (2014) Spontaneous activity governs olfactory representations in spatially organized habenular microcircuits. *Curr Biol* 24:434–439.
- Jhou TC, Fields HL, Baxter MG, Saper CB, Holland PC (2009) The rostromedial tegmental nucleus (rmtg), a GABAergic afferent to midbrain dopamine neurons, encodes aversive stimuli and inhibits motor responses. *Neuron* 61:786–800.
- Jia H, Rochefort NL, Chen X, Konnerth A (2011) In vivo two-photon imaging of sensory-evoked dendritic calcium signals in cortical neurons. *Nat Protoc* 6:28–35.
- Krishnan S, Mathuru AS, Kibat C, Rahman M, Lupton CE, Stewart J, Claridge-Chang A, Yen SC, Jesuthasan S (2014) The right dorsal

- habenula limits attraction to an odor in zebrafish. *Curr Biol* 24:1167–1175.
- Lee A, Mathuru AS, Teh C, Kibat C, Korzh V, Penney TB, Jesuthasan S (2010) The habenula prevents helpless behavior in larval zebrafish. *Curr Biol* 20:2211–2216.
- Li J, Shew WL (2020) Tuning network dynamics from criticality to an asynchronous state. *PLoS Comput Biol* 16:e1008268.
- Lin Q (2015) Using vertical migration of larval zebrafish to study non-image-forming light processing: opsin, neural circuits and neuro-modulators. PhD thesis, National University of Singapore.
- Marder E (2012) Neuromodulation of neuronal circuits: back to the future. *Neuron* 76:1–11.
- Marshall N, Timme NM, Bennett N, Ripp M, Lautzenhiser E, Beggs JM (2016) Analysis of power laws, shape collapses, and neural complexity: new techniques and MATLAB support via the NCC toolbox. *Front Physiol* 7:250.
- Matsumoto M, Hikosaka O (2007) Lateral habenula as a source of negative reward signals in dopamine neurons. *Nature* 447:1111–1115.
- Mazzucato L, Fontanini A, La Camera G (2016) Stimuli reduce the dimensionality of cortical activity. *Front Syst Neurosci* 10:11.
- Ostojic S (2014) Two types of asynchronous activity in networks of excitatory and inhibitory spiking neurons. *Nat Neurosci* 17:594–600.
- Pachitariu M, Stringer C, Dipoppa M, Schröder S, Rossi LF, Dagleish H, Carandini M, Harris KD (2017) Suite2p: beyond 10,000 neurons with standard two-photon microscopy. *Biorxiv* e061507.
- Palumbo F, Serneels B, Pelgrims R, Yaksi E (2020) The zebrafish dorsolateral habenula is required for updating learned behaviors. *Cell Rep* 32:108054.
- Pandey S, Shekhar K, Regev A, Schier AF (2018) Comprehensive identification and spatial mapping of habenular neuronal types using single-cell RNA-seq. *Curr Biol* 28:1052–1065.
- Ponce-Alvarez A, Jouary A, Privat M, Deco G, Sumbre G (2018) Whole-brain neuronal activity displays crackling noise dynamics. *Neuron* 100:1446–1459.e6.
- Priesemann V, Munk MH, Wibral M (2009) Subsampling effects in neuronal avalanche distributions recorded in vivo. *BMC Neurosci* 10:40.
- Ribeiro TL, Ribeiro S, Belchior H, Caixeta F, Copelli M (2014) Undersampled critical branching processes on small-world and random networks fail to reproduce the statistics of spike avalanches. *PLoS one* 9:e94992.
- Santos D, Luzio A, Coimbra AM (2017) Zebrafish sex differentiation and gonad development: a review on the impact of environmental factors. *Aquat Toxicol* 191:141–163.
- Softky WR, Koch C (1993) The highly irregular firing of cortical cells is inconsistent with temporal integration of random epsps. *J Neurosci* 13:334–350.
- Spitzner FP, Dehning J, Wiltling J, Hagemann A, Neto JP, Zierenberg J, Priesemann V (2021) Mr. estimator, a toolbox to determine intrinsic timescales from subsampled spiking activity. *PLoS One* 16:e0249447.
- Stephenson-Jones M, Floros O, Robertson B, Grillner S (2012) Evolutionary conservation of the habenular nuclei and their circuitry controlling the dopamine and 5-hydroxytryptophan (5-HT) systems. *Proc Natl Acad Sci U S A* 109:E164–E173.
- Thornton EW, Bradbury GE (1989) Effort and stress influence the effect of lesion of the habenula complex in one-way active avoidance learning. *Physiol Behav* 45:929–935.
- Van Vreeswijk C, Sompolinsky H (1996) Chaos in neuronal networks with balanced excitatory and inhibitory activity. *Science* 274:1724–1726.
- Wang RY, Aghajanian GK (1977) Physiological evidence for habenula as major link between forebrain and midbrain raphe. *Science* 197:89–91.
- Wiltling J, Priesemann V (2018) Inferring collective dynamical states from widely unobserved systems. *Nat Commun* 9:2325.
- Wiltling J, Priesemann V (2019a) Between perfectly critical and fully irregular: a reverberating model captures and predicts cortical spike propagation. *Cereb Cortex* 29:2759–2770.
- Wiltling J, Priesemann V (2019b) 25 years of criticality in neuroscience—established results, open controversies, novel concepts. *Curr Opin Neurobiol* 58:105–111.
- Wiltling J, Dehning J, Pinheiro Neto J, Rudelt L, Wibral M, Zierenberg J, Priesemann V (2018) Operating in a reverberating regime enables rapid tuning of network states to task requirements. *Front Syst Neurosci* 12:55.
- Zhang B-B, Yao Y-Y, Zhang H-F, Kawakami K, Du J-L (2017) Left habenula mediates light-preference behavior in zebrafish via an asymmetrical visual pathway. *Neuron* 93:914–928.
- Zhao H, Rusak B (2005) Circadian firing-rate rhythms and light responses of rat habenular nucleus neurons in vivo and in vitro. *Neuroscience* 132:519–528.